Heterostructured metal oxides-ZnO nanorods films prepared by SPPS route for photodegradation applications

Zexin Yu, Hatem Moussa, Meimei Liu, Raphael Schneider, Michel Moliere, Hanlin Liao

Heterostructured metal oxides-ZnO nanorods films prepared by SPPS route for photodegradation applications

Zexin Yu[a]*, Hatem Moussa[b], Meimei Liu[a], Raphaël Schneider[b]*, Michel Moliere[a], Hanlin Liao[a]

[a] ICB-LERMPS, UMR 6303, CNRS, UTBM, Université de Bourgogne Franche-Comté, 90010 Belfort, France

[b] Laboratoire Réactions et Génie des Procédés, Université de Lorraine, CNRS, LRGP,-F-54000 Nancy, France

* Corresponding author: Zexin Yu: *zexin.yu@utbm.fr;* Raphaël Schneider*: raphael.schneider@univ-lorraine.fr*

This work presents the first preparation using the Solution Precursor Plasma Spray process of heterostructured films associating ZnO nanorods (NRs) and various metal oxides (CuO, Fe_2O_3 and Co_3O_4) by Solution Precursor Plasma Spray process. These CuO/ZnO, Fe_2O_3/ZnO and Co_3O_4/ZnO films exhibit hierarchically chocolate sticks-like, dandelion-like or chrysanthemum-like surface morphologies. The heterostructure were confirmed by SEM, XRD, EDS and Raman analyses. The bandgaps of heterostructured films are narrower than that of pure ZnO. The CuO/ZnO film exhibits the highest photocatalytic activity both under UV and visible light irradiation for the degradation of the Orange II dye due to the homogenous distribution of CuO at the surface of ZnO. The high photocatalytic performances originate from the increased visible light absorption and from the effective separation of charge carriers in CuO/ZnO films compared to ZnO NRs.

Keywords: Solution precursor plasma spray; ZnO; nanorods; heterostructured films; hierarchical microstructure; photocatalytic degradation

1. Introduction

Due to the inadequate access to clean and fresh water, 1.2 billion people lack access to safe drinking water and 2.6 billion have little or no sanitation [1], which strongly points out the necessity and urgency of treating polluted water. Therefore, there is a growing interest worldwide in the development of photocatalytic degradation processes to remove organic pollutants since this process doesn't require any extra chemical reagent but simply employs semiconductor photocatalysts (such as TiO_2, ZnO and Fe_2O_3) and light [2-4]. However, to become an efficient photocatalyst in real applications, ZnO faces a barrier which lies in its light absorption, which is limited to the UV region due to its wide bandgap of 3.37 eV. In order to make ZnO suitable for harvesting and using visible light energy, coupling ZnO with semiconductors of lower bandgap like CuO, Fe_2O_3 or Co_3O_4 has been reported [5-9]. This strategy also allows an efficient separation of photogenerated electrons (e^-) and holes (h^+) and allows reaching high photocatalytic performances. 1-D ZnO nanostructures such as Nanorods (NRs) and Nanowires (NWs) with high aspect ratios have been shown to promote adequate charge separation due to their anisotropic morphology. In addition, it has been reported that the polar (002) crystal plane of ZnO exhibits better photocatalytic activity due to its positive charge that entails better absorption of hydroxyl (OH^-) ions. In the photocatalytic process, the OH^- ions are known to react with the photogenerated h^+ to generate hydroxyl (•OH) radicals that were demonstrated to play a key role in many photodegaradtions [10-12]. Especially, as far as the ZnO NRs morphology is concerned, increasing the exposure of (002) planes and the delocalization of electrons results in higher photocatalytic activity [13, 14]. Therefore, developing metal oxides coupled ZnO photocatalysts with hierarchal 1D microstructure is an efficient approach to improve the photodegradation performance.

Recently, heterostructured ZnO-based photocatalysts exhibiting well-shaped morphologies and complex phase compositions are mainly prepared via wet-chemical methods (i.e. hydrothermal, sol-gel, precipitation). However, these routes suffer from multi-steps, low yield and long duration [6, 15, 16]. Moreover, handling of nanopowder-formed photocatalysts will require tedious post-filtration steps and probably generate potential environmental and health risks from the nanoparticles after collecting [17-23]. Considering the practical applications of the photodegradation technology, the preparation of film-formed photocatalysts by a rapid one-step route is more attractive.

Among the various coating technologies, the solution precursor plasma spray (SPPS) process is a

promising alternative, benefiting from rapid single-step procedure, high flexibility and high production efficiency [24]. In the SPPS route, precursor solutions are used as feedstock and are heated and accelerated by a direct-current plasma generated by a primary gas (e.g. argon) and a secondary gas (e.g. hydrogen) to deposit the desired materials on the selected substrates [24, 25]. In this method, the injected salt solutions undergo a complex sequence of chemical and physical processes before depositing the final metal oxide films [26-28]. It is noteworthy that the photocatalytic metal oxide films are directly formed and the synthesis duration is only of several minutes. To our best knowledge, preparing heterostructured ZnO NRs films composed of NRs is a technologically challenging objective since the common microstructures of SPPS-deposited films are cauliflower-like microstructure and these films are composed of numerous irregularly shaped particles or flattens splats [27, 29, 30].

In this work, the use of the SPPS method was pioneered to directly build-up ZnO NRs based films coupled with CuO, Fe_2O_3, Co_3O_4. These films were characterized by scanning electron microscopy (SEM), X-ray diffraction (XRD), Raman spectroscopy and UV-visible spectrophotometer (UV-Vis). The photodegradation of the Orange II diazo dye under UV or visible light irradiation was selected to verify the photocatalytic activity of these ZnO NRs based films.

2. Experimental

2.1. Solution precursor preparation

Zinc acetate dihydrate ($Zn(CH_3COO)_2{\cdot}2H_2O$, Alfa Aesar, ACS 98.0–101.0%), copper(II) nitrate hemi(pentahydrate) ($Cu(NO_3)_2{\cdot}2.5H_2O$, Alfa Aesar, ACS, 98.0-102.0%), iron(III) nitrate nonahydrate ($Fe(NO_3)_3{\cdot}9H_2O$, Alfa Aesar, ACS, 98.0-101.0%) and cobalt(II) nitrate hexahydrate (($Co(NO_3)_3{\cdot}6H_2O$, Alfa Aesar ACS, 98.0-102.0%) were chosen as the precursor for formation of ZnO, CuO, Fe_2O_3 and Co_3O_4, respectively. The molar ratio of Cu/Zn, Fe/Zn and Co/Zn were fixed at 0.2 in the raw precursor solutions for depositing the CuO/ZnO, Fe_2O_3/ZnO and Co_3O_4/ZnO NRs films.

2.2. Plasma spray conditions

To process the aforementioned solution precursors, F4 plasma torch (Oerlikon Metco, Switzerland) was used as the heat source that was attached to a six-axis robotic arm (ABB, Switzerland) for precisely and automatically controlling the moving trajectory. The various precursor solutions used to prepare the

metal oxide coupled ZnO NRs films were driven by pressurized nitrogen flow through a stainless steel injector. The spraying parameters, namely the flow rates of primary gas (Ar) and secondary gas (H_2), the spraying distance, the deposition cycles and the moving velocity of the robotic arm were identical. Commercial alumina plates (33 x 34 x 2 mm) were used as the substrates. In order to obtain the hierarchical microstructured metal oxide composite films using the SPPS route, a spraying strategy was employed, as schematically illustrated in Fig.1. A $Zn(OAc)_2$ solution was firstly injected into the plasma plume to deposit ZnO NRs-structured films, followed by the injection of the metal-salt solution to form the targeted coupled-metal oxides. In order to protect the ZnO NRs before coupling, a period of ca. 1-2 minutes was observed before injecting the metal-salt solution precursors.

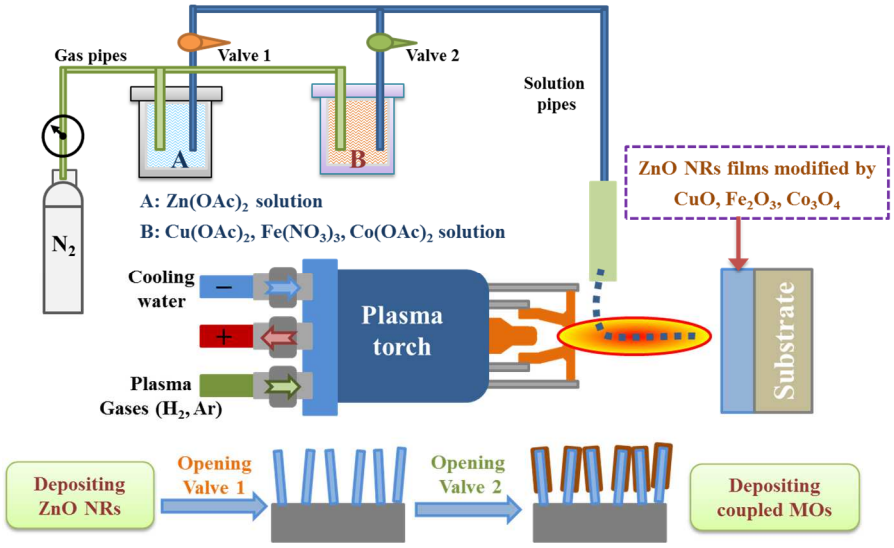

Fig. 1. Deposition strategy for the preparation of ZnO NRs coupled with metal oxides films via the SPPS process.

2.3. Characterization of the coatings

The surface morphologies of the resulting heterostructured CuO/ZnO, Fe_2O_3/ZnO and Co_3O_4/ZnO NRs films were firstly examined by scanning electron microscopy (SEM, JEOL, JSM-5800LV). The compositions of the samples were determined by X-ray diffraction (XRD, Bruker AXS D8 focus, Germany) using a cobalt anticathode (λ=1.78897 Å) and Raman spectrum (XploRA PLUS Raman Microscope, Horiba Jobin Yvon) with the excitation occurring at 532 nm. Their optical properties were evaluated by UV-visible absorption spectroscopy and diffuse reflectance spectroscopy using a UV–vis

spectrophotometer (Shimadzu, UV-2600). Then the corresponding optical energy bandgap values were estimated based on Kubelka-Munk equation, resorting to the Tauc plot method [31].

2.4. Photocatalytic testing

The photocatalytic performances of CuO/ZnO, Fe_2O_3/ZnO and Co_3O_4/ZnO NRs films were evaluated through the degradation of Orange II at room temperature under the UV and visible light irradiation, respectively. The UV light was produced by an Hg-Xe lamp with an intensity of 15 mW/cm^2 and the visible light was produced by a Xe lamp equipped with an ultraviolet cutoff filter ($\lambda > 420$ nm) and with an intensity of 7.5 mW/cm^2. A set of five identical film pieces representing in total 60 mg of photocatalysts was placed into a Petri dish containing 60 mL of the Orange II aqueous solution. Before irradiation, the liquid was magnetically stirred for 120 min in the dark to reach the adsorption-desorption equilibrium of the Orange II dye onto the films. During the subsequent irradiation procedure, 1 mL of the liquid was extracted at regular time intervals to estimate the remaining concentration of Orange II by measuring its UV-visible absorption at 485 nm (Thermo Scientific Evolution 220 spectrophotometer). The photodegradation percentage of Orange II was calculated as follows:

$$D(\%) = \frac{C_0 - C_t}{C_0} \times 100\% \qquad Eq(1)$$

where C_0 is the initial concentration of Orange II and C_t is the concentration of Orange II after irradiation time t, respectively.

3. Results and discussions

3.1. Characterization of surface morphology

Fig.2 displays the SEM for pure ZnO, CuO/ZnO, Fe_2O_3/ZnO and Co_3O_4/ZnO NR films under low and high magnifications. The pure ZnO films appear to be composed of well-shaped ZnO NRs (Fig.2a-c), which is in complete contrast to the conventional microstructures usually obtained via the SPPS process [27, 29, 30]. Using the same deposition procedure, metal oxides (CuO, Fe_2O_3 and Co_3O_4) were deposited and associated to the as-prepared ZnO NRs (Fig.2d-l), suggesting the formation of heterostructured films. However, due to the distinct chemical and physical properties of copper, iron

and cobalt species, CuO, Fe_2O_3 and Co_3O_4 exhibited different microstructures, which resulted in a variety of heterostructured metal-oxide films. For example, a chocolate sticks -like morphology could be observed for CuO/ZnO films (see Fig.2d-f), in which some of the CuO particles cover both the side and top surfaces of ZnO NRs. When comparing Fig.2a-c and Fig.2d-f, it can be seen that the smooth surface of the pure ZnO NRs became rough as a result of the deposition of CuO particles. In contrast, Fe_2O_3 particles were mainly found on the top of ZnO NRs, forming dandelion-like microstructures (Fig.2g-i), where the average size of Fe_2O_3 particles is about 100 nm. This phenomenon was confirmed by the XRD and Raman results and will be discussed below. Similarly, Fig.2j-l illustrates that the Co_3O_4 particles stack together on top of the ZnO NRs to form chrysanthemum-like microstructures. The size of the Co_3O_4 particles ranged from 100 to 300 nm. The backscattered electrons images for those heterostructured films are displayed in Fig. S1. Finally, it should be highlighted that CuO/ZnO, Fe_2O_3/ZnO and Co_3O_4/ZnO films exhibited hierarchical surface morphologies with high surface areas.

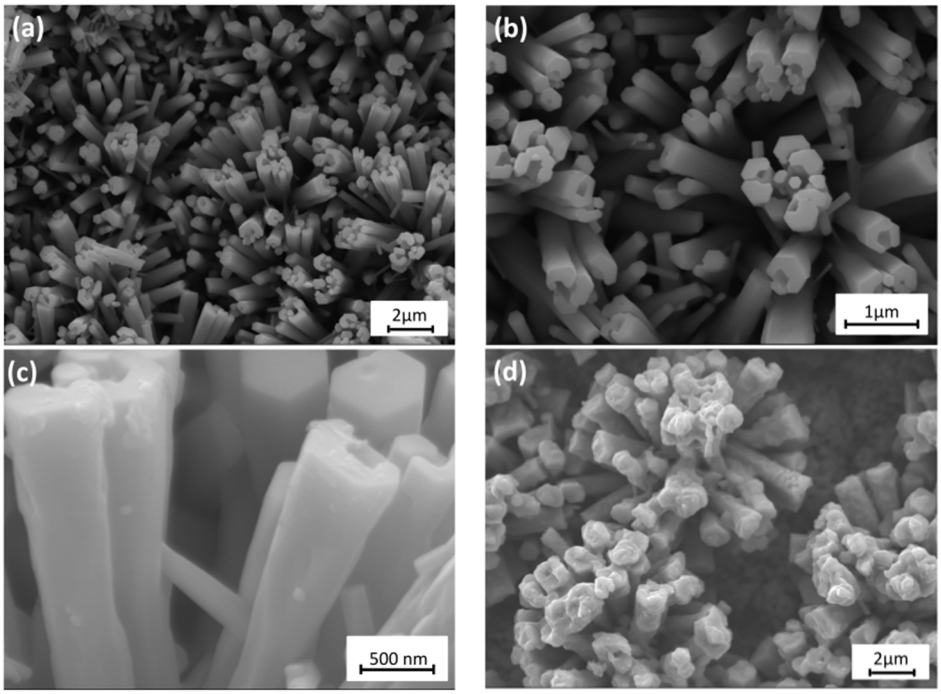

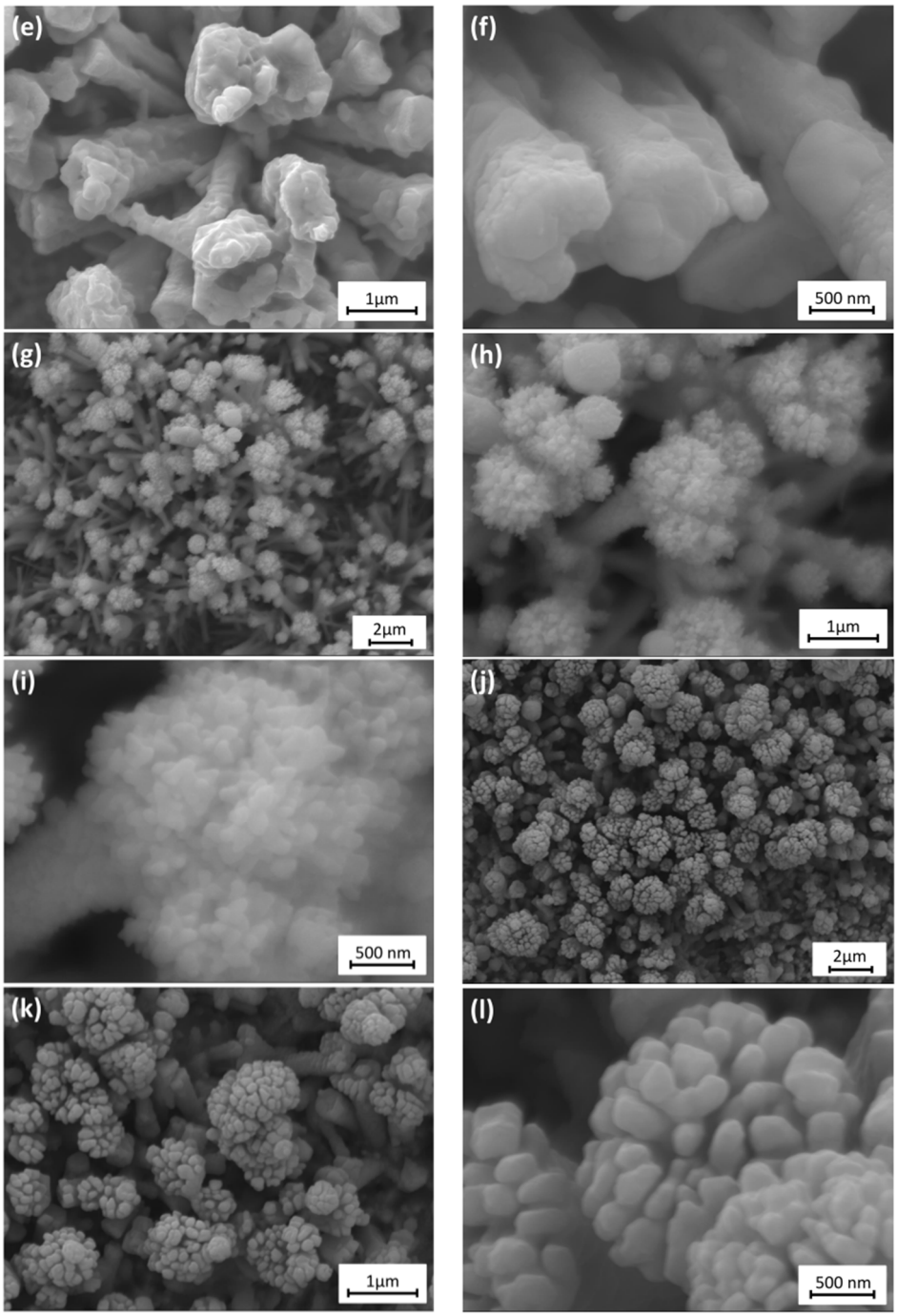

Fig.2. SEM images of (a-c) pure ZnO NRs films, (d-f) CuO/ZnO NRs films, (g-i) Fe_2O_3/ZnO NRs films and (j-l) Co_3O_4/ZnO NRs films under low and high magnifications.

In addition, to determine the distribution of ZnO and of the various coupled metal oxides in the heterostructured films, EDS analyses were conducted (Fig. 3-5). For each sample ~~type~~, two characteristic points were selected for analysis (Point 1 on the top and Point 2 side of the NRs). Fig. 3 confirms the coexistence of Cu and Zn elements in the CuO/ZnO NR sample. The Cu is present both on

the top of the ZnO stick and on the side of the ZnO stick, exhibiting similar intensities of both copper and zinc elements. It indicates that CuO is relatively uniformly decorated on the ZnO stick. By contrast, the ratios of Co/Zn and Fe/Zn determined on the top of stick or on the side of stick are obviously different (Fig. 4 and Fig. 5), suggesting highly non-uniform distribution of Co_3O_4 and Fe_2O_3 on the ZnO stick. These EDS results are in accordance with the previously described SEM images of Fe_2O_3/ZnO and Co_3O_4/ZnO NR films (Fig.2 g-l). In summary, all the CuO/ZnO, Fe_2O_3/ZnO and Co_3O_4/ZnO NR films exhibited hierarchical surface morphologies with high surface areas.

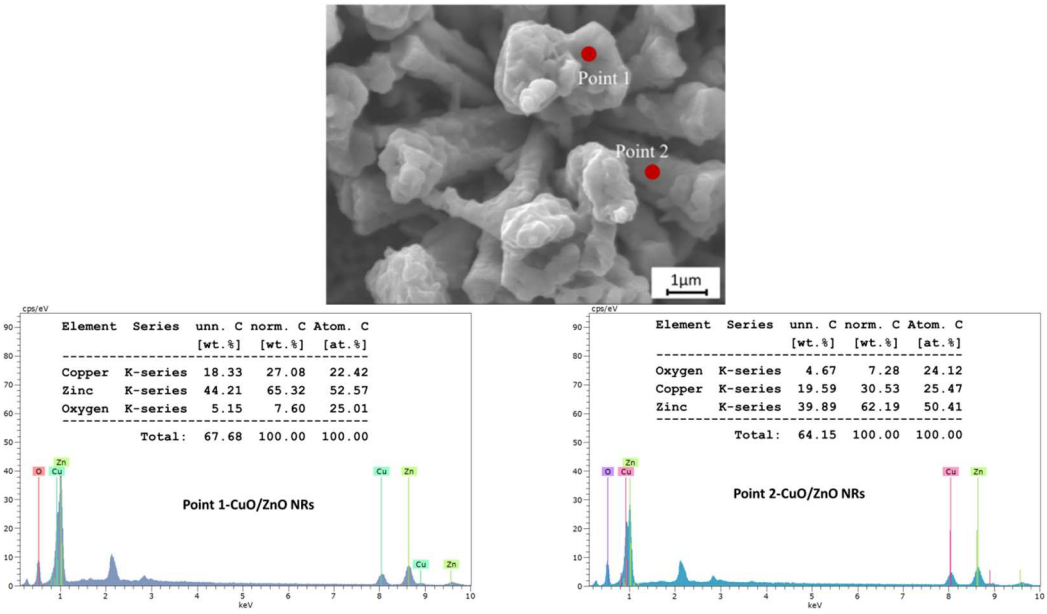

Fig. 3. EDS analysis of the CuO/ZnO film.

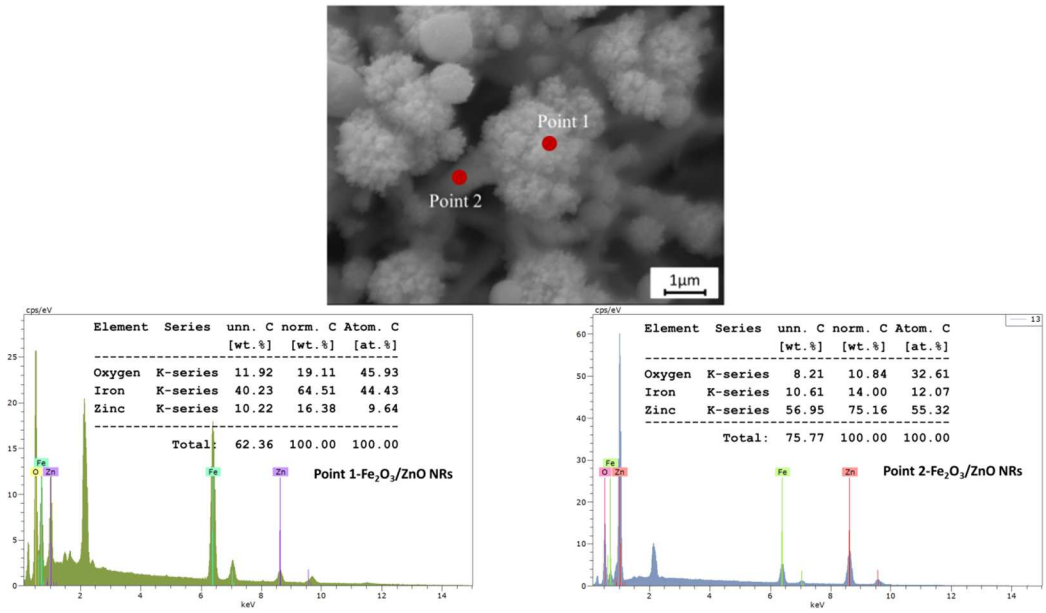

Fig. 4. EDS analysis of the Fe_2O_3/ZnO film.

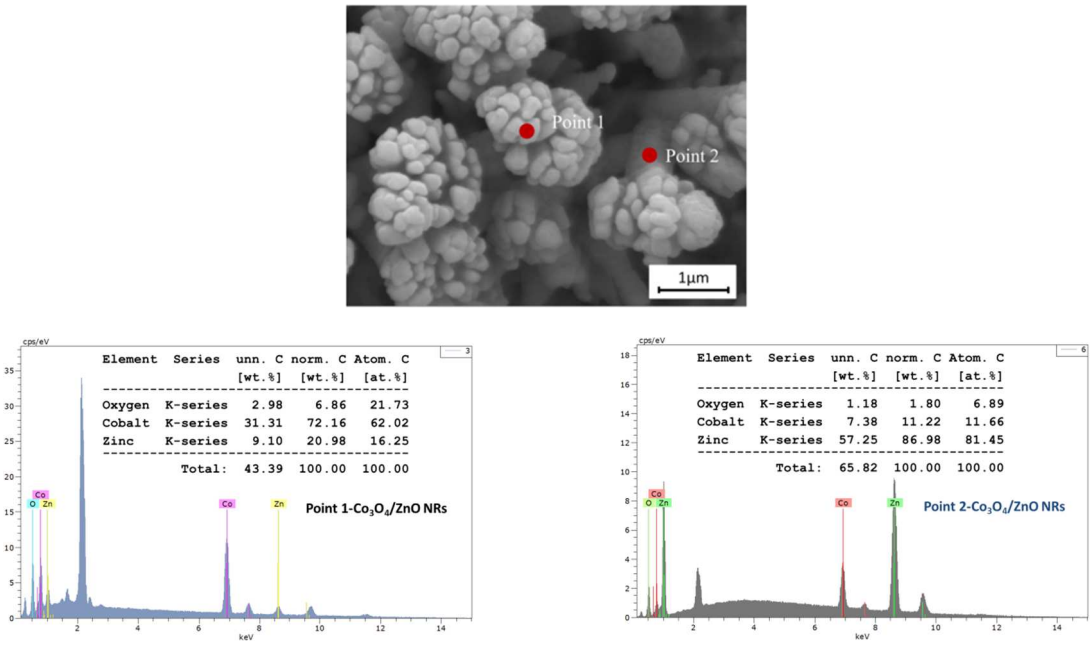

Fig. 5. EDS analysis of the Co_3O_4/ZnO film.

3.2. Composition of the ZnO based films

XRD patterns of the pure ZnO and of heterostructured CuO/ZnO, Fe_2O_3/ZnO and Co_3O_4/ZnO films are shown in Fig. 6. Due to the low thickness and to the porosity of these films, the underlying alumina substrates (PDF 81-2267) were also detected. For pure ZnO film, the XRD peaks of the standard hexagonal-wurtzite structure of ZnO (PDF 75-0576) were obtained. When using low concentrations (0.02M) of copper, iron and cobalt nitrates, low amounts of CuO (PDF 74-1021), Fe_2O_3 (PDF 85-0987) and Co_3O_4 (PDF 76-1802) can be observed in the XRD patterns (Fig. 6). In addition, due to the high temperatures of the in-flight particles and of the substrate in the SPPS process, $ZnFe_2O_4$ (PDF 73-1963) was also formed via a reaction between Fe_2O_3 and the pre-deposited ZnO film.

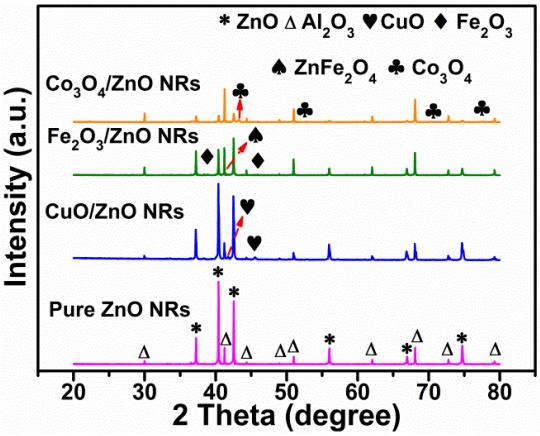

Fig.6. XRD patterns of pure ZnO NRs, CuO/ZnO NRs, Fe_2O_3/ZnO NRs and Co_3O_4/ZnO NRs films.

To obtain more information on the composition of the heterostructured films, Raman spectra were also recorded as shown in Fig.7. The peaks located at 332 cm^{-1}, 380 cm^{-1}, 437 cm^{-1} and 578 cm^{-1} can be assigned to the E_2 , A_{1TO} , E_1 , and $E_{2\ (high)}$ vibration modes of ZnO with the $P6_3mc$ symmetry, respectively (Fig. 7a) [32]. Similar to the XRD results, the vibration modes of the Al_2O_3 substrate at 416 cm^{-1}, 646 cm^{-1} and 748 cm^{-1} were also observed [33]. The characteristic peaks at 289 cm^{-1} and 627 cm^{-1} confirm the existence of CuO in CuO/ZnO NR films (Fig. 7b) [34]. In the Fe_2O_3/ZnO NRs sample (Fig. 7c), the peaks at 123 cm^{-1}, 144 cm^{-1}, 168 cm^{-1}, 229 cm^{-1}, 287 cm^{-1}, 510 cm^{-1}, 664 cm^{-1} and 839 cm^{-1} correspond to Fe_2O_3 [35, 36]. The *in situ* formation of $ZnFe_2O_4$ is confirmed by the two characteristic peaks at 206 cm^{-1} and 487 cm^{-1} [37]. Finally, the characteristic vibration modes of 189 cm^{-1}, 485 cm^{-1}, 520 cm^{-1}, 623 cm^{-1}, 690 cm^{-1} and 704 cm^{-1} can be seen for the Co_3O_4/ZnO NRs film (Fig. 7d) [38]. The phases of the targeted ZnO associated to CuO, Fe_2O_3 and Co_3O_4 were confirmed by XRD and Raman analyses.

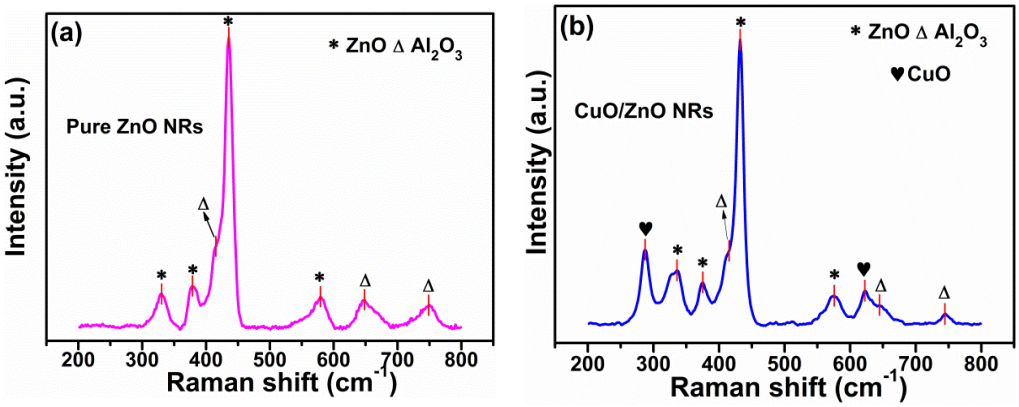

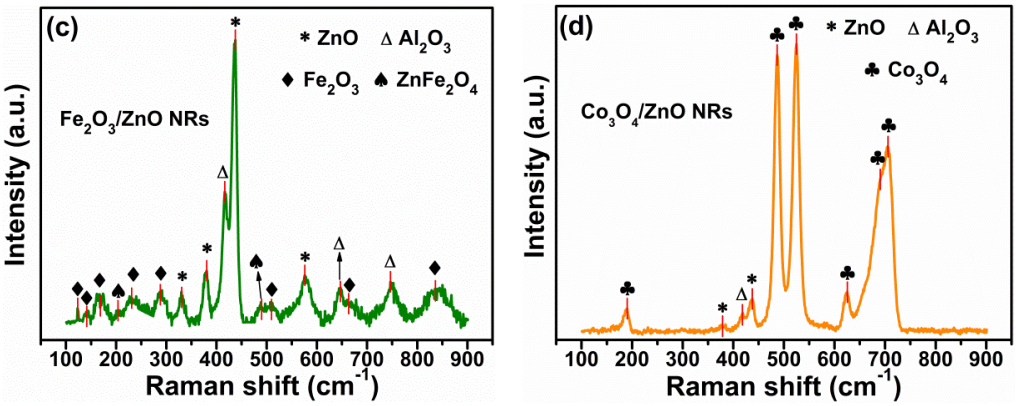

Fig.7 Raman spectrum of (a) pure ZnO NRs, (b) CuO/ZnO NRs, (c) Fe_2O_3/ZnO NRs and (d) Co_3O_4/ZnO NRs films.

3.3. Optical properties of heterostructured films

Fig. 8a-b show the UV-visible absorption spectra and diffuse reflectance spectra (DRS) of pure ZnO and of the heterostructured ZnO films, respectively. Only UV light (λ □ 368 nm) can be absorbed by pure ZnO due to its wide bandgap (3.37 eV in the bulk state). The heterostructured films show high absorption in the visible region of the light spectrum (see Fig. 8a), which should be beneficial to the visible-light-driven photocatalytic activity of the modified ZnO samples. The pure ZnO sample deposited via the SPPS route also exhibits an enhanced absorption (λ □ 450 nm) in the visible light range compared to bulk ZnO, likely due to the existence of oxygen vacancies at the surface of ZnO prepared via the SPPS process [24]. Using the Kubelka–Munk method [39] and the DRS results (Fig. 8b), the bandgap (*Eg*) values of the materials were determined by extrapolating the plots at $(F(R)\times h\nu)^2=0$ (Fig. 8c). The bandgaps were found to be 3.14, 2.77, 2.53 and 2.23 eV for pure ZnO, CuO/ZnO, Fe_2O_3/ZnO and Co_3O_4/ZnO NR films, respectively.

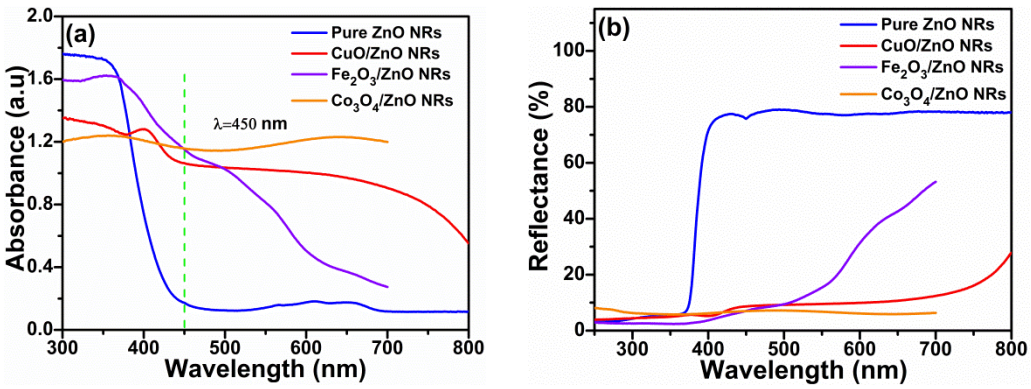

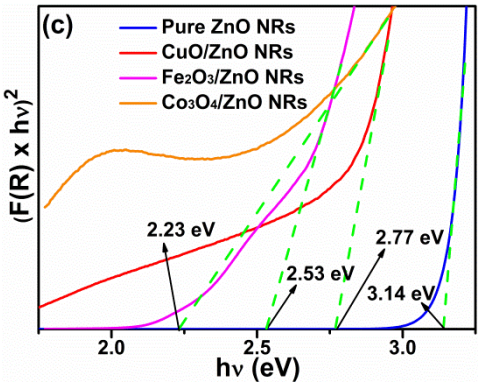

Fig. 8. (a) UV-visible absorption spectra and (b) UV-visible diffuse reflectance spectra of pure ZnO and heterostructured ZnO films and (c) Plot of $(F(R \times h\nu)^2$ vs hν of pure ZnO NRs, CuO/ZnO NRs, Fe_2O_3/ZnO NRs and Co_3O_4/ZnO NRs films.

3.4. Photodegradation performance under UV light

The photocatalytic activity of pure ZnO and heterostructured ZnO NRs films were first evaluated for the degradation of the Orange II dye under UV light irradiation. The evolutions of the UV-visible absorption spectra of the Orange II are shown in Fig. 9a-d. The characteristic absorption peak of Orange II located at 485 nm gradually decreases with the irradiation time, indicating the bleaching of the dye. The plots of C_t/C_0 versus irradiation time for all samples are shown in Fig. 9e. The CuO/ZnO NRs film exhibits the highest photocatalytic efficiency (97.4% degradation after 300 min), while 92.5% of the dye were degraded using the pure ZnO NRs film. The photodegradation efficiencies of Fe_2O_3/ZnO NRs and Co_3O_4/ZnO NRs films are lower (83.2% and 82.6% after 300 min irradiation, respectively). Indeed, it is commonly accepted that the efficient transfer of photogenerated electrons/holes is a requirement for photocatalytic degradation. Although both pure Fe_2O_3 and $ZnFe_2O_4$ exhibit excellent visible-light responses, Fe_2O_3 is limited by a high recombination rate of charge carriers and by its relatively low oxidation ability [39, 40]. $ZnFe_2O_4$ and Co_3O_4 also suffer from a modest photoelectric conversion [9, 41]. Moreover, in light of the SEM and EDS results previously described, Fe_2O_3, $ZnFe_2O_4$ and Co_3O_4 particles were mainly stacked on top of ZnO NRs nanostructures in the Fe_2O_3/ZnO and Co_3O_4/ZnO films, suggesting a weak contact with ZnO. We assume that the lower photocatalytic performances of Fe_2O_3/ZnO and Co_3O_4/ZnO films originate from the weak contact between Fe_2O_3 or Co_3O_4 and ZnO. For the CuO/ZnO film, CuO particles were demonstrated to be uniformly distributed at the surface of ZnO NRs, which favors the creation of a heterojunction between these materials and thus the delocalization of photogenerated holes and electrons.

Fig. 9f shows that the photocatalytic degradation of Orange II with ZnO and the heterostructured ZnO-based films fits the pseudo-first-order kinetics $\ln (C_0/C) = kt$, where C_0 and C are the

concentrations of the dye at t = 0 and t, respectively, and k is the rate constant. The rate constant k can be classified as follows: CuO/ZnO NRs > pure ZnO NRs > Fe_2O_3/ZnO NRs > Co_3O_4/ZnO NRs. In light of the above investigation, it can be concluded that the distribution of metal oxides in the photocatalyst plays a key important role in the photocatalytic activity of heterostructured films prepared via the SPPS process. Further works devoted to control this distribution will be undertaken in a near future.

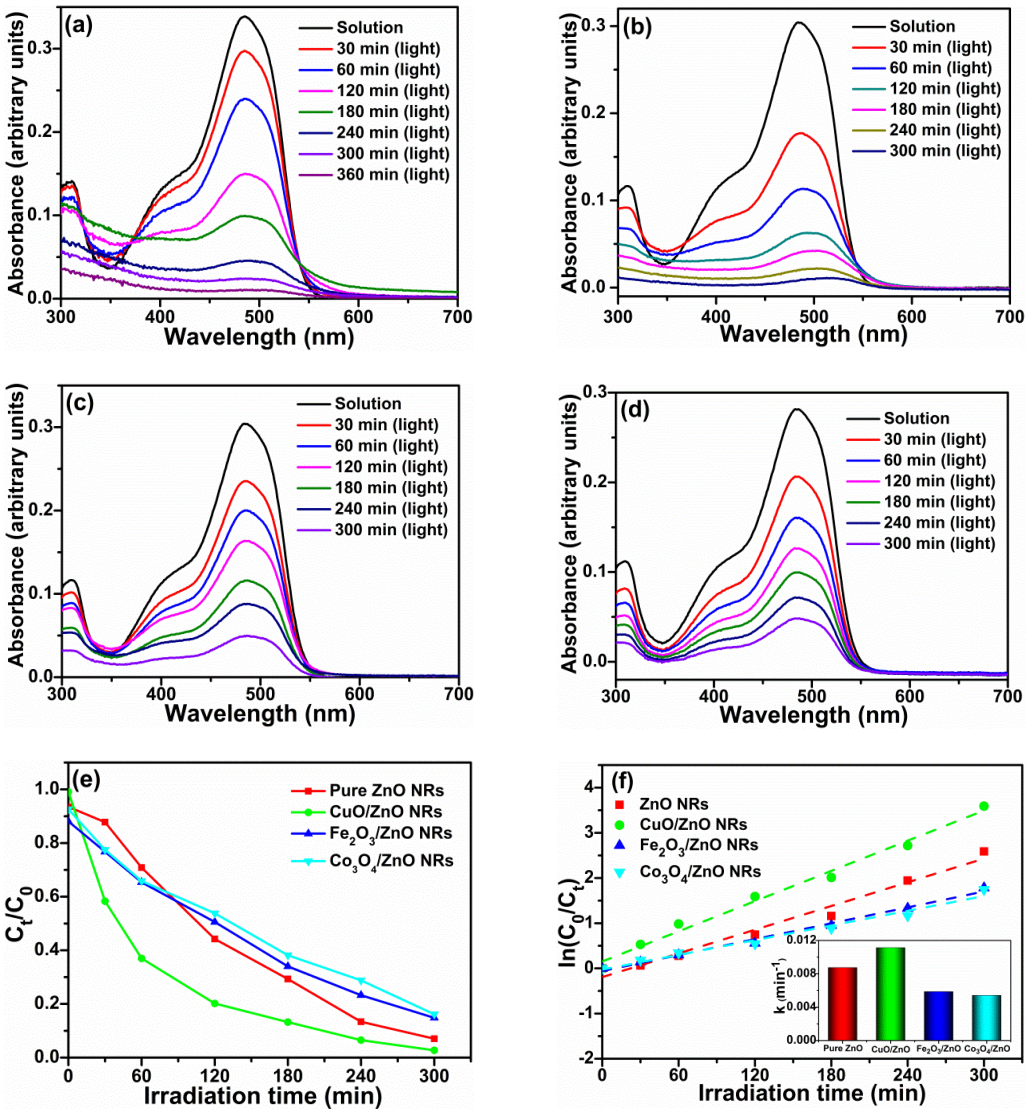

Fig. 9. UV-visible absorption spectra of Orange II during its photodegradation under UV light in the presence of (a) pure ZnO, (b) CuO/ZnO, (c) Fe_2O_3/ZnO and (d) Co_3O_4/ZnO films, (e) photodegradation performances of the catalysts and (f) the pseudo-first-order kinetics of Orange II degradation under UV light for pure ZnO and heterostructured films.

3.5. Photocatalytic activity under visible light

In order to further evaluate the photocatalytic activity of heterostructured films, the photodegradation performances under visible light were also investigated. The time-evolutions of the UV-visible absorption spectra of Orange II are shown in Fig.10a-d. A faster decrease of the characteristic peak of Orange II at 485 nm was observed for all heterostructured films compared to pure ZnO NRs. Fig. 10e displays the plots of C_t/C_0 versus irradiation time for all films. The CuO/ZnO NRs films exhibit the highest visible-light-driven photodegradation efficiency (41.8%) within 360 min, followed by the Co_3O_4/ZnO NRs sample (39.3%) and Fe_2O_3/ZnO NRs films (28.4%). All heterostructured films exhibit improved photodegradation performances than pure ZnO NRs samples (9.8%), which is mainly related to their ability to harvest visible light. Results obtained are consistent with those obtained under UV light irradiation and further demonstrate that an optimal contact between the two metal oxides favors the photocatalytic activity. The reaction kinetics for pure ZnO and the heterostructured films are shown in Fig. 10f. The reaction constants of CuO/ZnO NRs, Fe_2O_3/ZnO NRs and Co_3O_4/ZnO NRs films are 5.5, 3.2 and 4.5 times higher than that of pure ZnO NRs, respectively.

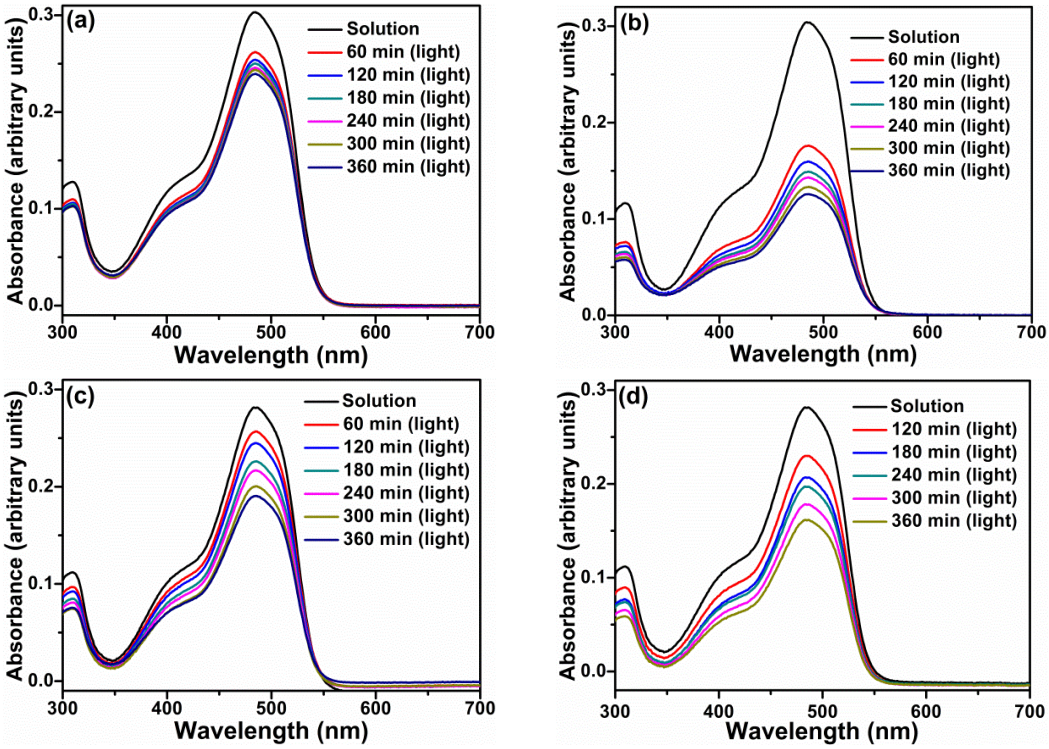

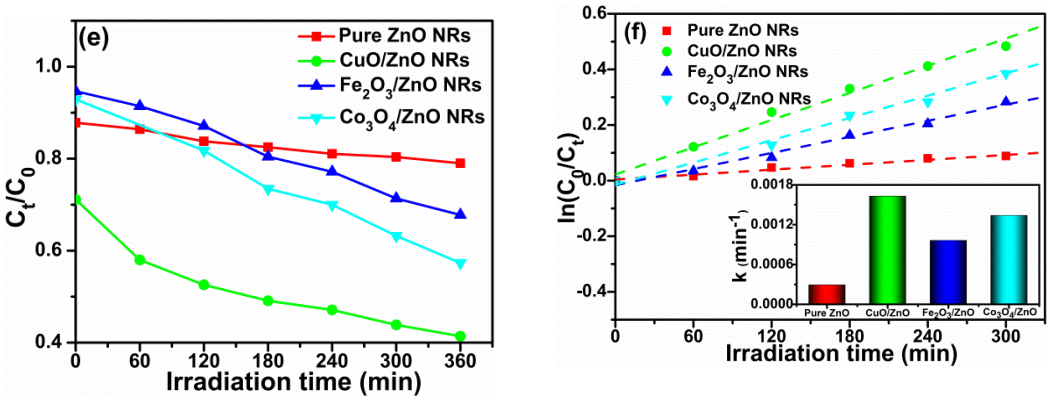

Fig. 10. (a-d) UV-visible spectra of Orange II during its photodegradation under visible light in the presence of pure ZnO and heterostructured films, (e) photodegradation performance in function of the irradiation time and (f) the pseudo-first-order kinetics of Orange II.

3.6. Photocatalytic mechanism

ZnO is an n-type semiconductor, while CuO is p-type semiconductor. The p-n heterojunction between these materials should favor the separation of holes and electrons. The valence band (VB) and the conduction band (CB) edge position of ZnO and CuO were estimated according to their absolute electronegativity. Based on previous studies, the relationship between conduction (E_{CB}) and valence (E_{VB}) band edges energies and the electronegativity can be expressed as follows [42]:

$$E_{VB} = \chi - E^e + 0.5E_g \qquad Eq(2)$$

$$E_{CB} = E_{VB} - E_g \qquad Eq(3)$$

where χ is the absolute electronegativity of the semiconductor expressed as the geometric mean of the absolute electronegativity of the constituent atoms, E^e is the energy of free electrons in the hydrogen scale (~4.5 eV) and E_g is the energy bandgap of the semiconductor. The χ values for ZnO and CuO are 5.79 and 5.81 Ev. The bandgaps of ZnO and CuO are 3.12 and 1.70 eV [43]. Table 1 summarizes the calculated E_{VB} and E_{CB} values on. A possible charge transfer mechanism in heterostructured films is illustrated in Fig. 11.

Table 1. Absolute electronegativity, E_V and E_C values for ZnO and CuO (vs NHE).

semiconductor	χ (eV)	E_g (eV)	E_{CB} (eV)	E_{VB} (eV)
ZnO	5.79	3.12	-0.27	2.85
CuO	5.81	1.70	-0.44	2.14

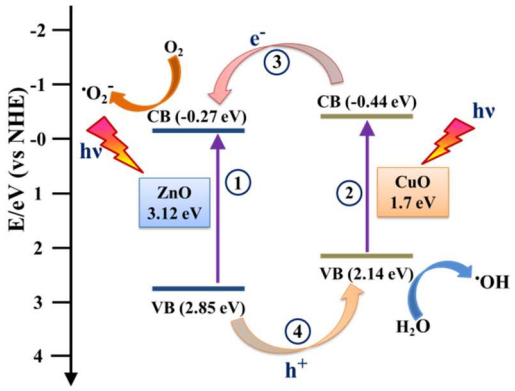

Fig. 11. Schematic band structure of the CuO/ZnO photocatalyst and of the charge transfer between CuO and ZnO under light irradiation.

Firstly, under the UV light irradiation, both CuO and ZnO are excited (steps 1 and 2 and reaction *i*). Due to the p-n heterojunction between ZnO and CuO, the photogenerated electrons transfer from the CB of CuO to the CB of ZnO. In the meantime, the photogenerated holes migrate in the opposite direction from the VB of ZnO to that of CuO (steps 3 and 4 and reaction *ii*). These transfers limit the electron/hole recombination both in CuO and ZnO and thus increase the photocatalytic activity. The holes accumulated in the VB of CuO react with water molecules to generate hydroxyl radicals (•OH) (reaction *iii*). Simultaneously, electrons accumulated in the CB of ZnO are scavenged by dissolved oxygen molecules and produce superoxide anions ($O_2^{\bullet-}$) (reaction *iv*). Hydroxyl and superoxide radicals oxidize the Orange II dye (reactions v and reaction vi).

Under visible light irradiation, only CuO is efficiently excited. The electrons in the CB of CuO transfer to the CB of ZnO. As previously, these electrons react with oxygen while holes in the VB of CuO react with water.

$$CuO/ZnO + h\nu \rightarrow CuO/ZnO\left(h^{+}_{(vb)} + e^{-}_{(cb)}\right) \quad (i)$$

$$CuO/ZnO\left(h^{+}_{(vb)} + e^{-}_{(cb)}\right) \rightarrow CuO\left(h^{+}\right) + ZnO\left(e^{-}\right) \quad (ii)$$

$$ZnO(e^{-}) + O_2 \rightarrow O_2^{\cdot-} \quad (iii)$$

$$CuO\left(h^{+}\right) + H_2O \rightarrow \cdot OH + H^{+} \quad (iv)$$

$$O_2^{\cdot-} + \text{Orange II} \rightarrow \text{Intermediates} \rightarrow \text{Degradation Products} \quad (v)$$

$$\cdot OH + \text{Orange II} \rightarrow \text{Intermediates} \rightarrow \text{Degradation Products} \quad (vi)$$

4. Conclusion

It is the pioneering report that heterostructured metal oxides films (CuO, Fe_2O_3 and Co_3O_4) coupled to ZnO nanorods were efficiently prepared by the SPPS technology. The CuO/ZnO, Fe_2O_3/ZnO and Co_3O_4/ZnO films obtained exhibit hierarchical chocolate-stick, dandelion and chrysanthemum-like morphologies, respectively. Among these films, CuO was demonstrated to be uniformly distributed on the top and on the side of pre-deposited ZnO nanorods, while Fe_2O_3 and Co_3O_4 were mainly stacked on the top of ZnO nanorods. The heterostructured films exhibit enhanced absorption in the visible region compared to pure ZnO. Under UV light irradiation, the CuO/ZnO film exhibits the highest photocatalytic activity for the degradation of the Orange II dye, likely due to optimal heterojunction constructed between CuO and ZnO that favors the charge transfers. Under visible light, CuO/ZnO, Fe_2O_3/ZnO and Co_3O_4/ZnO films exhibit a 5.5, 3.2 and 4.5 times higher activity than pure ZnO, respectively. This study not only reveals the capability of SPPS for the direct deposition of heterostructured metal oxides films, but also demonstrates that the distribution of the metal oxide plays a key role in the photocatalytic performance.

Acknowledgement

The authors, Zexin YU and Meimei LIU, gratefully appreciate to the support from the China Scholarship Council (Grant No. 201504490038 and Grant No. 201604490072).

References

[1] M.A. Shannon, P.W. Bohn, M. Elimelech, J.G. Georgiadis, B.J. Marinas, A.M. Mayes 2008 Science and technology for water purification in the coming decades *Nature* **452** 301

[2] M.M. Khin, A.S. Nair, V.J. Babu, R. Murugan, S. Ramakrishna 2012 A review on nanomaterials for environmental remediation *Energy Environ. Sci.* **5** 8075

[3] Z. Cai, Y. Sun, W. Liu, F. Pan, P. Sun, J. Fu 2017 An overview of nanomaterials applied for removing dyes from wastewater *Environ. Sci. Pollut. Res. Int.* **24** 15882-15904

[4] A. Rivera, K. Tanaka, T. Hisanaga 1993 Photocatalytic degradation of pollutant over TiO_2 in different crystal structures *Applied Catalysis B: Environmental* **3** 37-44

[5] J. Xie, Z. Zhou, Y. Lian, Y. Hao, P. Li, Y. Wei 2015 Synthesis of α-Fe_2O_3/ZnO composites for photocatalytic degradation of pentachlorophenol under UV–vis light irradiation *Ceram. Int.* **41** 2622-2625

[6] S. Harish, J. Archana, M. Sabarinathan, M. Navaneethan, K.D. Nisha, S. Ponnusamy, C. Muthamizhchelvan, H. Ikeda, D.K. Aswal, Y. Hayakawa 2017 Controlled structural and compositional characteristic of visible light active ZnO/CuO photocatalyst for the degradation of organic pollutant *Appl. Surf. Sci.* **418** 103-112

[7] K. Mageshwari, D. Nataraj, T. Pal, R. Sathyamoorthy, J. Park 2015 Improved photocatalytic activity of ZnO coupled CuO nanocomposites synthesized by reflux condensation method *J. Alloys Compd.* **625** 362-370

[8] C. Dong, X. Xiao, G. Chen, H. Guan, Y. Wang 2015 Synthesis and photocatalytic degradation of methylene blue over pn junction Co_3O_4/ZnO core/shell nanorods *Mater. Chem. Phys.* **155** 1-8

[9] L. Sun, R. Shao, L. Tang, Z. Chen 2013 Synthesis of $ZnFe_2O_4$/ZnO nanocomposites immobilized on graphene with enhanced photocatalytic activity under solar light irradiation *J. Alloys Compd.* **564** 55-62

[10] A. Mclaren, T. Valdes-Solis, G. Li, S.C. Tsang 2009 Shape and size effects of ZnO nanocrystals on photocatalytic activity *J. Am. Chem. Soc.* **131** 12540-12541

[11] A. Dodd, A. McKinley, T. Tsuzuki, M. Saunders 2009 Tailoring the photocatalytic activity of nanoparticulate zinc oxide by transition metal oxide doping *Mater. Chem. Phys.* **114** 382-386

[12] E.S. Jang, J.H. Won, S.J. Hwang, J.H. Choy 2006 Fine tuning of the face orientation of ZnO crystals to optimize their photocatalytic activity *Adv. Mater.* **18** 3309-3312

[13] X. Zhang, J. Qin, Y. Xue, P. Yu, B. Zhang, L. Wang, R. Liu 2014 Effect of aspect ratio and surface defects on the photocatalytic activity of ZnO nanorods *Sci. Rep.* **4** 4596

[14] A. Leelavathi, G. Madras, N. Ravishankar 2013 Origin of enhanced photocatalytic activity and photoconduction in high aspect ratio ZnO nanorods *PCCP* **15** 10795-10802

[15] P. Sathishkumar, R. Sweena, J.J. Wu, S. Anandan 2011 Synthesis of CuO-ZnO nanophotocatalyst for visible light assisted degradation of a textile dye in aqueous solution *Chem. Eng. J.* **171** 136-140

[16] B. Li, Y. Wang 2010 Facile synthesis and photocatalytic activity of ZnO–CuO nanocomposite *Superlattices Microstruct.* **47** 615-623

[17] N.K. Dey, M.J. Kim, K.-D. Kim, H.O. Seo, D. Kim, Y.D. Kim, D.C. Lim, K.H. Lee 2011 Adsorption and photocatalytic degradation of methylene blue over TiO_2 films on carbon fiber prepared by atomic layer deposition *J. Mol. Catal. A: Chem.* **337** 33-38

[18] S. Dosta, M. Robotti, S. Garcia-Segura, E. Brillas, I.G. Cano, J.M. Guilemany 2016

Influence of atmospheric plasma spraying on the solar photoelectro-catalytic properties of TiO_2 coatings *Applied Catalysis B: Environmental* **189** 151-159

[19] C. Guillard, J. Disdier, C. Monnet, J. Dussaud, S. Malato, J. Blanco, M.I. Maldonado, J.-M. Herrmann 2003 Solar efficiency of a new deposited titania photocatalyst: chlorophenol, pesticide and dye removal applications *Applied Catalysis B: Environmental* **46** 319-332

[20] H.-J. Wang, Y.-Y. Sun, C.-F. Wang, Y. Cao 2012 Controlled synthesis, cytotoxicity and photocatalytic comparison of ZnO films photocatalysts supported on aluminum matrix *Chem. Eng. J.* **198-199** 154-162

[21] J.-J. Wu, C.-H. Tseng 2006 Photocatalytic properties of nc-Au/ZnO nanorod composites *Applied Catalysis B: Environmental* **66** 51-57

[22] Y. Xu, M. Shen 2008 Fabrication of anatase-type TiO_2 films by reactive pulsed laser deposition for photocatalyst application *J. Mater. Process. Technol.* **202** 301-306

[23] Z. Mengyue, C. Shifu, T. Yaowu 1995 Photocatalytic degradation of organophosphorus pesticides using thin films of TiO_2 *J. Chem. Technol. Biotechnol.* **64** 339-344

[24] Z. Yu, H. Moussa, M. Liu, R. Schneider, M. Moliere, H. Liao 2018 Solution precursor plasma spray process as an alternative rapid one-step route for the development of hierarchical ZnO films for improved photocatalytic degradation *Ceram. Int.* **44** 2085-2092

[25] Z.X. Yu, Y.Z. Ma, Y.L. Zhao, J.B. Huang, W.Z. Wang, M. Moliere, H.L. Liao 2017 Effect of precursor solutions on ZnO film via solution precursor plasma spray and corresponding gas sensing performances *Appl. Surf. Sci.* **412** 683-689

[26] P. Fauchais, R. Etchart-Salas, V. Rat, J.F. Coudert, N. Caron, K. Wittmann-Ténèze 2008 Parameters Controlling Liquid Plasma Spraying: Solutions, Sols, or Suspensions *J. Therm.*

Spray Technol. **17** 31-59

[27] P. Fauchais, G. Montavon 2009 Latest Developments in Suspension and Liquid Precursor Thermal Spraying *J. Therm. Spray Technol.* **19** 226-239

[28] P. Fauchais, V. Rat, J.F. Coudert, R. Etchart-Salas, G. Montavon 2008 Operating parameters for suspension and solution plasma-spray coatings *Surf. Coat. Technol.* **202** 4309-4317

[29] G. Bertolissi, C. Chazelas, G. Bolelli, L. Lusvarghi, M. Vardelle, A. Vardelle 2012 Engineering the Microstructure of Solution Precursor Plasma-Sprayed Coatings *J. Therm. Spray Technol.* **21** 1148-1162

[30] L. Pawlowski 2009 Suspension and solution thermal spray coatings *Surf. Coat. Technol.* **203** 2807-2829

[31] R. López, R. Gómez 2011 Band-gap energy estimation from diffuse reflectance measurements on sol–gel and commercial TiO_2: a comparative study *J. Sol-Gel Sci. Technol.* **61** 1-7

[32] J. Wang, Y. Xia, Y. Dong, R. Chen, L. Xiang, S. Komarneni 2016 Defect-rich ZnO nanosheets of high surface area as an efficient visible-light photocatalyst *Applied Catalysis B: Environmental* **192** 8-16

[33] P. Li, M. Lei, W. Tang 2010 Raman and photoluminescence properties of α-Al_2O_3 microcones with hierarchical and repetitive superstructure *Mater. Lett.* **64** 161-163

[34] M.H. Chou, S.B. Liu, C.Y. Huang, S.Y. Wu, C.L. Cheng 2008 Confocal Raman spectroscopic mapping studies on a single CuO nanowire *Appl. Surf. Sci.* **254** 7539-7543

[35] J. López-Sánchez, A. Serrano, A. Del Campo, M. Abuín, O. Rodríguez de la Fuente, N.

Carmona 2016 Sol–gel synthesis and micro-raman characterization of ε-Fe_2O_3 micro-and nanoparticles *Chem. Mater.* **28** 511-518

[36] Y. El Mendili, J.F. Bardeau, N. Randrianantoandro, A. Gourbil, J.M. Greneche, A.M. Mercier, F. Grasset 2011 New evidences of in situ laser irradiation effects on γ - Fe_2O_3 nanoparticles: a Raman spectroscopic study *J. Raman Spectrosc.* **42** 239-242

[37] Q. Xu, J. Feng, L. Li, Q. Xiao, J. Wang 2015 Hollow $ZnFe_2O_4/TiO_2$ composites: High-performance and recyclable visible-light photocatalyst *J. Alloys Compd.* **641** 110-118

[38] M. Rashad, M. Rüsing, G. Berth, K. Lischka, A. Pawlis 2013 CuO and Co_3O_4Nanoparticles: Synthesis, Characterizations, and Raman Spectroscopy *Journal of Nanomaterials* **2013** 1-6

[39] M. Niu, F. Huang, L. Cui, P. Huang, Y. Yu, Y. Wang 2010 Hydrothermal synthesis, structural characteristics, and enhanced photocatalysis of SnO_2/α-Fe_2O_3 semiconductor nanoheterostructures *ACS nano* **4** 681-688

[40] M. Mishra, D.-M. Chun 2015 α-Fe_2O_3 as a photocatalytic material: A review *Applied Catalysis A: General* **498** 126-141

[41] H. Chen, W. Liu, Z. Qin 2017 ZnO/$ZnFe_2O_4$ nanocomposite as a broad-spectrum photo-Fenton-like photocatalyst with near-infrared activity *Catalysis Science & Technology* **7** 2236-2244

[42] A. Naseri, M. Samadi, N.M. Mahmoodi, A. Pourjavadi, H. Mehdipour, A.Z. Moshfegh 2017 Tuning composition of electrospun ZnO/CuO nanofibers: toward controllable and efficient solar photocatalytic degradation of organic pollutants *The Journal of Physical Chemistry C* **121** 3327-3338

[43] Y. Xu, M.A. Schoonen 2000 The absolute energy positions of conduction and valence bands of selected semiconducting minerals *Am. Mineral.* **85** 543-556

Figure captions:

Fig.1. Deposition strategy for the preparation of ZnO NRs coupled with metal oxides films via the SPPS process.

Fig.2. SEM images of (a-c) pure ZnO NRs films, (d-f) CuO/ZnO NRs films, (g-i) Fe_2O_3/ZnO NRs films and (j-l) Co_3O_4/ZnO NRs films under low and high magnifications.

Fig. 3. EDS analysis of the CuO/ZnO film.

Fig. 4. EDS analysis of the Fe_2O_3/ZnO film.

Fig. 5. EDS analysis of the Co_3O_4/ZnO film.

Fig. 6. XRD patterns of pure ZnO NRs, CuO/ZnO NRs, Fe_2O_3/ZnO NRs and Co_3O_4/ZnO NRs films.

Fig. 7. Raman spectrum of (a) pure ZnO NRs, (b) CuO/ZnO NRs, (c) Fe_2O_3/ZnO NRs and (d) Co_3O_4/ZnO NRs films.

Fig. 8. (a) UV-visible absorption spectra and (b) UV-visible diffuse reflectance spectra of pure ZnO and heterostructured ZnO films and (c) Plot of $(F(R \times h\nu)^2$ vs $h\nu$ of pure ZnO NRs, CuO/ZnO NRs, Fe_2O_3/ZnO NRs and Co_3O_4/ZnO NRs films.

Fig. 9 UV-visible absorption spectra of Orange II during its photodegradation under UV light in the presence of (a) pure ZnO, (b) CuO/ZnO, (c) Fe_2O_3/ZnO and (d) Co_3O_4/ZnO films, (e) photodegradation performances of the catalysts and (f) the pseudo-first-order kinetics of Orange II degradation under UV light for pure ZnO and heterostructured films.

Fig. 10. (a-d) UV-visible spectra of Orange II during its photodegradation under visible light in the presence of pure ZnO and heterostructured films, (e) photodegradation performance in function of the irradiation time and (f) the pseudo-first-order kinetics of Orange II.

Fig. 11. Schematic band structure of the CuO/ZnO photocatalyst and of the charge transfer between CuO and ZnO under light irradiation.

Table captions:

Table 1. Absolute electronegativity, E_V and E_C values for ZnO and CuO (vs NHE).